JNTM JOURNAL of NEW TECHNOLOGY and MATERIALS

Journal of New Technology and Materials

Vol. 14, No. 2 (2024), 21–33

RESEARCH ARTICLE

Biorthogonal Doublon–Holon Dipole Tomography for Collective Skin Localization in Non-Reciprocal Spin-Fermion Chains

Vincent Marks[1] and R. A. Sulaiman[2,*]

[1]University of Surrey, Guildford GU2 7XH, Surrey, UK

*Correspondence: rsuleman7@gmail.com

Received date: July 28, 2024; Accepted date: November 30, 2024

Abstract

The study of non-Hermitian lattice models has emerged as indispensable to the characterization of engineered quantum materials, arrays of optical elements, electric circuits, and cold atomic simulators where dissipative processes or non-reciprocal transport modify the connection between bulk band structure and surface states. When considering interacting fermionic systems, the non-Hermitian skin effect can no longer be detected through total charge accumulation, since correlations lead to the formation of composite charge defects that affect the mobile degrees of freedom. Here we introduce a novel biorthogonal doublon-holon dipole tomography technique for detecting correlated skin localization effects in a non-reciprocal spin-1/2 Hubbard chain. The procedure breaks down each individual eigenstate into left-right normalized doublon density, holon density, defect dipole polarization, quasiparticle separation, connected doublon-holon covariance, and flux dependence of spectral complexity. The procedure is used to analyze half-filled and holon-doped Hubbard chains at $L = 8$, $N = 8$, $N = 7$, both periodic and open boundary conditions, $A = 0.3$, representative couplings $U/t = 0$ and $U/t = 10$, and $U/t \to 20$ interaction scans. Our findings show that in the half-filled no-pair Mott sector, charge polarization is maintained at a weak level, while in finite doublon-holon sectors, boundary stretched dipole textures appear and increase in intensity proportionally to the charge defects. As interactions are turned on, the smooth weak-correlation imbalance is replaced by a staircase of states ordered according to doublon-holon occupancy; in the case of the doped chain, an unpaired holon provides an additional boundary-active channel, resulting in a response biased towards an odd integer hierarchy. Flux-torsion spectroscopy establishes a connection between the texture and complex eigenvalue loops, allowing us to identify exceptional state reconfiguration events where complex eigenvalue branches turn real. These tools enable an excitation resolved exploration of collective non-Hermitian skin effect physics in interacting quantum materials.

Keywords: non-Hermitian quantum materials, non-reciprocal Hubbard chain, doublon–holon excitation, collective skin effect, biorthogonal tomography, point-gap topology, engineered materials

1 Introduction

Non-Hermitian physics has evolved to become the language for the description of material systems wherein dissipation, gain, non-reciprocal hopping, reservoir interactions, radiation losses, or measurement feedback effects do not enter the model as small external perturbations. In a Hermitian lattice system, the set of eigenvalues is real and the profile of a state can be found using an orthonormal set of wave functions. In a non-Hermitian lattice system, however, the spectrum may wind into loops in the complex plane, the left and right eigenvectors cease to be related by a simple Hermitian conjugation, and the degeneracy points correspond to an exceptional-point mechanism in which both eigenstates and eigenvalues collapse together [1–3]. Such non-trivial properties are no longer purely theoretical. They serve as a tool for understanding photonic lattices, topolectrical circuits, acoustic or mechanical metamaterials, quantum devices, and synthetic atom systems in which controlled loss and non-reciprocity play a role in their operation [4–6]. Therefore, in the development of new technologies and novel materials, the important aspect is no longer whether a model of interest

belongs to the class of non-Hermitian Hamiltonians but, more precisely, whether there exists a measurable excitation type responsible for a boundary effect induced by non-Hermiticity.

The non-Hermitian skin effect provides the best example in this regard. In the open-chain setup, a non-reciprocal lattice may give rise to a significant population of localized boundary states despite being extended on periodic boundaries. The skin effect is closely associated with winding in the spectrum, generalized Brillouin zones, and non-Bloch bulk–boundary correspondence [7–9]. It was understood later that the skin effect is actually topological within the framework of the non-Hermitian system: an open boundary response is characterized by winding of the point gap around a reference level under flux insertion [10, 11]. Although the above discussion concerns the single-particle scenario, one still needs to ask the question: what happens when the objects of interest are not mere particles but rather charge excitations generated by correlation?

The case becomes more complicated when considering interacting many-body systems. Fermion exclusion, Mott-like suppression, spin exchange, and interaction energy may preclude total particle density from becoming a reliable indicator of localization. Nevertheless, several works have shown that non-Hermitian point-gap topology survives interactions and many-body spectra retain winding even in the regime in which the single-particle approach fails [12–14]. On the other hand, Hubbard-type systems have shown that interactions may change the character of the non-Hermitian skin effect, either suppressing it entirely or relocating and reshaping the effect [15]. Related research in the realm of interacting non-reciprocal systems includes investigation of bound pairs and correlated channels in terms of their directional dynamics. Furthermore, the problem of skin effect has been considered in real space in order to understand the competition between correlation effects and the boundary amplification of a state [16–18]. Thus, the current literature demonstrates the need for a diagnostic tool based on the excitation identity of a localized boundary state.

The simplest model that allows for investigating such a distinction is that of the spin-1/2 Hubbard chain. In the half-filled regime, strongly repulsive interactions lead to low-energy configurations being singly occupied. However, an asymmetric hopping term in a non-Hermitian model cannot localize the entire density of particles in the half-filled regime because of the local constraint imposed by Mott physics. Nevertheless, excited charge sectors include doublon and holon excitations. A doublon is a site with two electrons occupying it whereas a holon represents a vacancy with respect to singly occupied sites. Thus, a doublon–holon pair constitutes a neutral but polarizable excitation. In a non-reciprocal chain, such a pair is capable of stretching itself into a dipole along the boundary of the chain. The study presented in this paper is devoted to exploring this particular excitation.

An overall winding number is clearly insufficient for achieving this goal since it indicates presence of the skin effect in a spectrum but tells nothing about the specific charge sector or defect configuration underlying the effect. Similarly, a density imbalance test shows presence of localized boundary states in the form of an imbalance of the total density but again provides no indication of the identity of the defects involved. Thus, a diagnosis technique for the skin effect in interacting non-Hermitian models should necessarily include a spectral topological analysis alongside biorthogonal state-resolved local observables.

The use of biorthogonal states is justified since right eigenvectors by themselves tend to exaggerate a localized component of a state due to the amplification effect. The left eigenvector provides the second half of a state pair necessary to calculate observables consistently. As a result, it becomes possible to explore the behavior of local observables depending on how close to an exceptional point and on how large the amplification in each eigenstate is [4, 19]. The set of biorthogonal observables employed in the present work includes the dipole and separation distances for defects along with connected covariances and flux-torsion spectral winding. These five observables provide a tomography procedure that translates an eigenproblem for a non-Hermitian many-body chain into a defect-based visualization.

Figure 1 illustrates the flow chart of this procedure. It should be noted that the procedure starts with a biorthogonal state pair, then uses local projections onto individual charges in order to measure defects, constructs dipole moments and separation lengths, evaluates connected covariances, and finally applies flux insertion into the spectrum to measure its winding. The purpose of the procedure is to determine the defects and excitations responsible for skin physics rather than deduce the localization of the states based on the imbalance.

The importance of the above procedure lies in preventing collapse of the skin effect analysis to a single observable such as the imbalance test or spectral winding. A localized boundary state should be regarded as a state that has both defects localized at the edges and spectral winding. It becomes especially crucial in a close vicinity of exceptional regions in which eigenvalues, eigenvector conditioning, and local observables behave similarly.

In summary, this paper addresses the following question: Is it possible to use defect-resolved non-Hermitian dipole moment to analyze a skin effect in the interacting non-reciprocal spin chain? The answer proposed below is positive. There will be an imbalance due to the existence of doublon–holon excitations but no pair contribution means that the chain will be weakly polarized. Increasing the interaction strength leads to emergence of localized boundary defects in the form of dipole stretching. Further addition of one electron gives rise to an unpaired holon and the response appears in an odd chain. Flux-torsion spectral analysis connects the spatial and spectral phenomena.

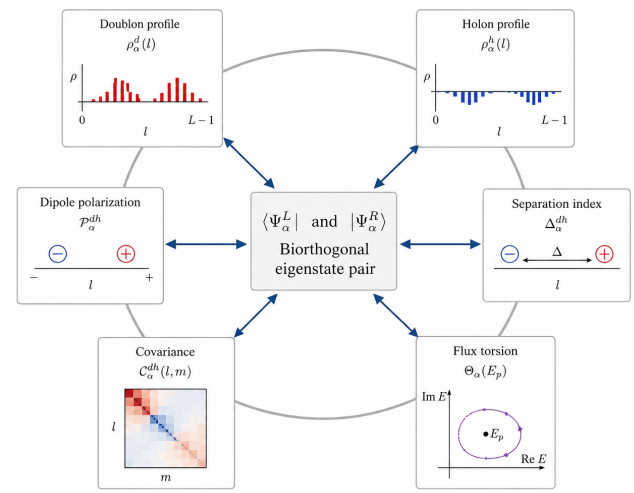

Figure 1. Defect-resolved procedure for translating an eigenstate of a non-Hermitian many-body model into a visual representation of its localization and spectral winding. Each step of the procedure starts from the biorthogonal eigenpair $\langle\Psi_\alpha^L|$ and $|\Psi_\alpha^R\rangle$, projects onto the doublon and holon charge sectors, determines the polarization direction and the separation distance between defects, finds whether the defects come from the same correlated excitation, and checks participation of the state in the flux-induced winding in the spectral plane.

2 Model and computational settings

The model is a one-dimensional spin-1/2 non-reciprocal Hubbard chain with directional bias and on-site repulsion. The Hamiltonian is

$$H(A,U,\phi)=\sum_{l=0}^{L-2}\sum_{\sigma=\uparrow,\downarrow} t\left(e^{A}c_{l+1,\sigma}^{\dagger}c_{l,\sigma}+e^{-A}c_{l,\sigma}^{\dagger}c_{l+1,\sigma}\right)+\sum_{l=0}^{L-1}Un_{l,\uparrow}n_{l,\downarrow}+H_B(\phi), \tag{1}$$

where $c_{l,\sigma}^{\dagger}$ ($c_{l,\sigma}$) creates (annihilates) a fermion of spin σ at site l, $n_{l,\sigma}=c_{l,\sigma}^{\dagger}c_{l,\sigma}$, and t is the hopping integral. Parameter U determines the strength of on-site repulsion, while A describes a directional hopping bias through the imaginary vector potential.

Hamiltonian (1) encodes two competing physics that drive the whole paper. Directional factors e^{A} and e^{-A} imply open-boundary polarization of the wavefunction amplitude. On the other hand, the Hubbard term prefers zero double occupancy, thereby organizing the energy spectrum based on the number of doublon–holon excitations. Thus, the skin effect is not driven by hopping non-reciprocity alone but by its interplay with the interaction-induced charge structure of many-body eigenstates.

Setting $H_B=0$ corresponds to open boundary conditions. Periodic and twisted boundary conditions are incorporated using

$$H_B(\phi)=\sum_{\sigma} t\left(e^{A+i\phi}c_{0,\sigma}^{\dagger}c_{L-1,\sigma}+e^{-A-i\phi}c_{L-1,\sigma}^{\dagger}c_{0,\sigma}\right). \tag{2}$$

In this expression, ϕ denotes the boundary phase $\phi=0$ corresponds to the periodic boundary condition.

Eq. (2) plays a double role in the present context. Firstly, neglecting $H_B(\phi)$ opens the boundaries and therefore reveals the skin effect through the localization pattern in the bulk. Secondly, adding $H_B(\phi)$ with a tunable phase turns the boundary into a tool for branch spectroscopy, allowing one to investigate the spectral winding $E_\alpha(\phi)$ over one full cycle. Comparing open and twisted boundary spectra thus constitutes the basis for connecting boundary polarization to exceptional-point topological winding.

Finite basis of the many-body Hilbert space is fixed by the total particle number N and by the total magnetization S_z. An individual basis state can be written as

$$|\Psi_n\rangle=\prod_{j=1}^{N}c_{l_{nj},\sigma_{nj}}^{\dagger}|0\rangle. \tag{3}$$

Here l_{nj} and σ_{nj} label the site and spin of the jth particle in the nth occupation basis state.

Eq. (3) not only describes the computational basis choice but provides the physical picture of the occupancy in each basis vector. Specifically, the occupation picture allows for decomposition of the eigenvector coefficients into the weights of localized holes and localized doublons. Without the basis in terms of occupations, it would be hard to classify the

sectors in terms of no pairs, one pair, two pairs, and doped cases.

Table 1 presents the summary of the physical and numerical parameters used in the work. The chain size is $L = 8$ in all the considered systems. Two cases with particle numbers $N = 8$ and $N = 7$ are studied: the former represents a half-filled setting while the latter involves a doped situation with a single hole added to the system. Interaction strengths are chosen to represent two contrasting limits of $U/t = 0$ and $U/t = 10$ to illustrate mixing of sectors in absence of interactions and sector separation for large U/t. Moreover, we consider $U/t = 20$ in order to detect exceptional-state reorganization. The representative value of imaginary vector potential that defines non-reciprocity is $A = 0.3$. Finally, all results are obtained with open, periodic and twisted boundaries.

Table 1. Physical and numerical parameters used in the biorthogonal analysis of the doublon-holon problem. Final column shows the rationale for including each numerical parameter in the study.

Parameter name	**Values or sectors**	**Diagnostic role**
Lattice size	$L = 8$	Enables finite-chain diagnostics of defect localization, covariance mapping, and left-right imbalance across the sites.
Particle number	$N = 8$ and $N = 7$	Separates half-filled neutral system from doped setting with one mobile holon added prior to pair formation.
Interaction strength	$U/t = 0$, $U/t = 10$, and $U/t = 20$	Reveals mixing of sectors in absence of repulsion and separation in strong interaction limit.
Imaginary vector potential	$A = 0.3$	Determines the direction of polarization.
Boundary condition	Open, periodic, and twisted boundaries	Enables discrimination between skin polarization and spectral winding through independent diagnostics.
Flux range	$0 \leq \phi \leq 2\pi$	Enables branch-resolved complex spectroscopy over one full cycle.
Excitation sectors	$N_d = 0, 1, 2, 4$	Distinguish no-pair, one-pair, two-pairs, and four-pairs charge-defect sectors.
Representative symmetry sector	$k = 0$, $S_z = 0$	Provides a basis for branch tracking and comparison of eigenstate textures.
Observed imbalance pattern	Smooth arch at $U/t = 0$; staircase at $U/t = 10$; sequence of odd points for $N = 7$	Supplies the phenomenology that needs to be decomposed into pair-mediated and defect-mediated terms.

Table 1 is included in the paper for clarity of interpretation and reproducibility of the results. Each entry in Table 1 includes a rationale for the specific choice. In particular, one should note that the difference between $N = 8$ and $N = 7$ is crucial because it discriminates a pair-mediated channel from a single-defect one. In addition, the distinction between open and twisted boundaries is necessary as spectral winding with no localization or polarization without spectral winding cannot provide a proof of collective skin effect.

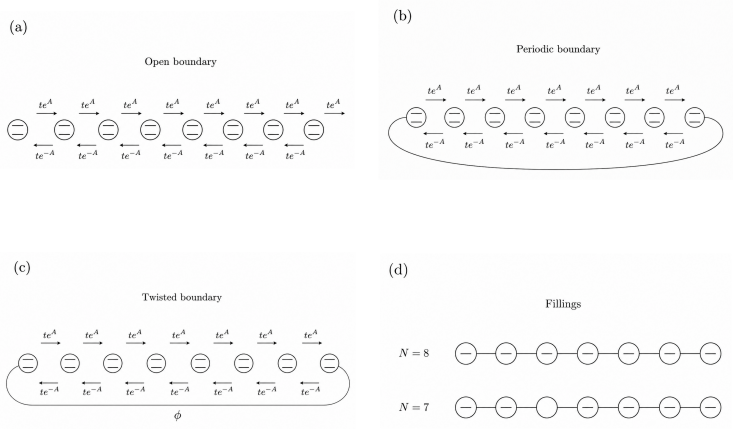

Figure 2. Boundary and filling combinations for the non-reciprocal Hubbard chain. Boundaries can be open, periodical, or twisted. Filled systems are half-filled $N = 8$ or one-hole doped $N = 7$. Open boundaries reveal edge localization, periodical boundaries close the chain without introducing any phase, and twisted boundaries introduce the boundary phase ϕ.

Figure 2 visualizes the different choices of the parameters from Table 1. This figure splits all combinations of boundary implementations and fillings to show the reader where and how to apply diagnostics of skin effect and exceptional-point topological winding.

Main lesson of Figure 2 is that a single model Hamiltonian can be understood in two ways: either as an open real-space problem or as a twisted spectral problem. The two fillings then decide whether the mobile boundary-active object is necessarily a doublon–holon pair or can also be an unpaired holon.

3 Biorthogonal doublon–holon dipole tomography

In a non-Hermitian setting, right and left eigenvectors fulfill

$$H|\Psi_\alpha^R\rangle = E_\alpha|\Psi_\alpha^R\rangle, \qquad \langle\Psi_\alpha^L|H = E_\alpha\langle\Psi_\alpha^L|, \tag{4}$$

and the eigenvectors obey

$$\langle\Psi_\alpha^L|\Psi_\beta^R\rangle = \delta_{\alpha\beta}. \tag{5}$$

Eqs. (4) and (5) define the measurement basis used in the paper. Right eigenstate carries information about the propagated wave pattern, while the left eigenstate determines the dual vector required to make a consistent expectation value. This is necessary because a right eigenvector can be exponentially amplified by the boundary, although the associated biorthogonal observable possesses a more intricate defect content.

Local projectors for the doublons and holons are

$$D_l = n_{l,\uparrow}n_{l,\downarrow}, \qquad Q_l = (1-n_{l,\uparrow})(1-n_{l,\downarrow}), \tag{6}$$

where D_l picks up the doubly occupied sites, while Q_l corresponds to vacancies. These operators define the analysis framework with respect to charge defects rather than total particle density. This is the crucial point that lets us distinguish the Mott-like no-pair sector from an excited sector with actual doublon–holon contents.

The corresponding defect biorthogonal densities are

$$d_\alpha(l) = \langle\Psi_\alpha^L|D_l|\Psi_\alpha^R\rangle, \qquad h_\alpha(l) = \langle\Psi_\alpha^L|Q_l|\Psi_\alpha^R\rangle. \tag{7}$$

In Eq. (7), each eigenstate is assigned a local structure. The expectation value defined in this way uses the left–right metric of the problem instead of only right vectors. In this case, one can obtain the natural distribution of the defects without misinterpreting exponential amplifications in the boundary states.

In a similar manner, non-Hermitian expectation values can be complex. Hence, the spatial tomography relies on the following normalized defect probabilities,

$$\rho_\alpha^d(l) = \frac{|d_\alpha(l)|}{\sum_{m=0}^{L-1}|d_\alpha(m)|}, \qquad \rho_\alpha^h(l) = \frac{|h_\alpha(l)|}{\sum_{m=0}^{L-1}|h_\alpha(m)|}, \tag{8}$$

provided that their denominator does not vanish. Such normalization separates where the defect resides and what total amount of defect exists in the eigenstate. Otherwise, it would incorrectly identify a high-defect sector as a localized one due to a higher total charge defect weight. States with very low defect probability are analyzed separately to avoid meaningless normalized profiles.

First among the three diagnostics introduced in this work is the doublon–holon dipole polarization,

$$\mathcal{P}_\alpha^{dh} = \frac{1}{L-1}\sum_{l=0}^{L-1}(2l-L+1)\left[\rho_\alpha^d(l)-\rho_\alpha^h(l)\right]. \tag{9}$$

Sign of $\mathcal{P}_\alpha^{dh}$ depends on the ordering of the sites and sign of A, while its magnitude shows how strong doublon and holon defects are displaced relative to each other. Vanishing of $\mathcal{P}_\alpha^{dh}$ can indicate lack of defects or symmetry between them. Therefore, this quantity should always be used in combination with the distance separation measure and covariation rather than considered as a standalone order parameter.

The second measure is the normalized quasiparticle separation,

$$\Delta_\alpha^{dh} = \frac{1}{L-1}\sum_{l,m=0}^{L-1}|l-m|\rho_\alpha^d(l)\rho_\alpha^h(m). \tag{10}$$

Measure in Eq. (10) calculates the average separation between two defect distributions. This quantity is useful when there is more than one configuration of the charge defects giving rise to multiple terms that could cancel out in the dipole moment calculation. Large Δ_α^{dh} value along with small value of $\mathcal{P}_\alpha^{dh}$ means separated defects that do not have precisely aligned orientations within each component. On the contrary, large values of both quantities imply stretched boundary dipole.

The third diagnostic is the normalized particle-density imbalance,

$$\eta_\alpha = \frac{1}{N}\left[\sum_{L/2\le l<L} \rho_\alpha^n(l) - \sum_{0\le l<L/2} \rho_\alpha^n(l)\right], \tag{11}$$

where

$$\rho_\alpha^n(l) = \frac{\left|\langle\Psi_\alpha^L|\sum_\sigma n_{l,\sigma}|\Psi_\alpha^R\rangle\right|}{\sum_{m=0}^{L-1}\left|\langle\Psi_\alpha^L|\sum_\sigma n_{m,\sigma}|\Psi_\alpha^R\rangle\right|}. \tag{12}$$

The imbalance η_α is deliberately retained even though the paper focuses on doublons and holons. It provides the conventional density-polarization signal against which the defect-resolved quantities are tested. The normalization by N makes the half-filled and doped chains comparable, while Eq. (12) keeps the density profile in the same biorthogonal metric as the defect profiles.

The final diagnostic is the connected doublon–holon covariance,

$$\mathcal{C}_\alpha^{dh}(l,m) = \langle\Psi_\alpha^L|D_l Q_m|\Psi_\alpha^R\rangle - d_\alpha(l)h_\alpha(m). \tag{13}$$

A high covariance value indicates correlation, i.e., an association between finding a doublon at one end of the chain and a holon at another. Such off-diagonal ridge or corner-to-corner covariance is the definitive evidence of a skin dipole being an elongated excitation and not simply an accidental superposition of locally charge polarized states.

The fifth diagnostic is the flux insertion dependence of spectral topology. Given an eigenstate with eigenvalue branch $E_\alpha(\phi)$, its flux torsion with respect to some local point-gap reference energy E_p is defined as

$$\Theta_\alpha(E_p) = \frac{1}{2\pi}\int_0^{2\pi} \frac{\partial}{\partial\phi}\arg\left[E_\alpha(\phi) - E_p\right]\,\mathrm{d}\phi. \tag{14}$$

The key difference between this definition and that used previously is that Eq. (14) applies to individual branches, whereas the previous definitions apply to entire spectral lineshapes. Therefore, it addresses the question of whether a given eigenstate, carrying a skin texture, indeed traces out a closed loop with nontrivial topology.

As a state approaches an exceptional point, its identity may flip, and the torsion becomes a measure of spectral reorganization instead of the continuity of one state. In such cases, only the presence of flux torsion is meaningful.

4 Numerical protocol and reviewer-level quality controls

The analysis is built up from four interdependent steps. First, eigenstates at half-filling are ordered according to the strength of their dominant doublon-holon texture. For each eigenstate, the quantities $\rho_\alpha^d(l)$, $\rho_\alpha^h(l)$, $\mathcal{P}_\alpha^{dh}$, Δ_α^{dh}, η_α, and $\mathcal{C}_\alpha^{dh}(l,m)$ are calculated. It allows identifying whether an eigenstate is charge inert, density-polarized, or truly dipolar.

Second, the sector structure is analyzed at $U/t = 0$ and $U/t = 10$ and compared. Since, at $U/t = 0$, configuration space does not distinguish between doublon counts and states of different local charge distribution are freely mixed, doublon number does not represent a robust organizing principle. On the other hand, at $U/t = 10$, interaction energy separates charge sectors according to defect number, and the tomography of an ideal dipole is expected to yield a staircase with clearly identifiable sectors.

Third, the eigenvalues are tracked through $0 \le \phi \le 2\pi$, and the corresponding flux torsions are computed. By comparing the latter with open-boundary dipole observables, we decide whether a branch of complex flux winding corresponds to an eigenstate with a defect-based dipole skin localization.

Finally, the doped case, with $N = 7$, is investigated. The existence of at least one holon in the lowest charge sector makes it impossible to separate skin localization driven by charge defects from simple holon–doublon pairs. The total density-based test is blind to this distinction, but the doublon–holon tomography is not.

Multiple quality controls are needed. The eigenvectors should be traced continuously through flux insertion, in order to exclude branch switching artifacts from the calculations of flux torsions. The denominator in Eq. (8) should be tracked to ensure that no artificial normalizations take place for no-pair states. Near exceptional points, the left–right overlap matrix should be monitored, to avoid excessive exaggeration of spatial distributions due to biorthogonal normalization. At weak interactions, the labels are taken to be dominant characters.

5 Results and discussion

5.1 Half-filled Mott sector and defect-suppression of skin response

First, we consider the half-filled chain within the no-pair sector. This sector is characterized by low doubly occupied or doubly unoccupied sites and therefore carries little real doublon or holon weight. Non-reciprocal hopping still applies, but there is no charge defect available to it. As a consequence, the no-pair sector should not exhibit strong charge polarization despite the Hamiltonian being non-Hermitian.

Figure 3 shows the diagnostic results. The doublon and holon weights are small and diffusely distributed. The charge profile is balanced between the two ends of the chain, with the density imbalance approaching zero, and the covariance has a negligible off-diagonal contribution. This is not a failure of non-reciprocity; it proves that the half-filled Mott-like sector is too defect-lean to support skin texture.

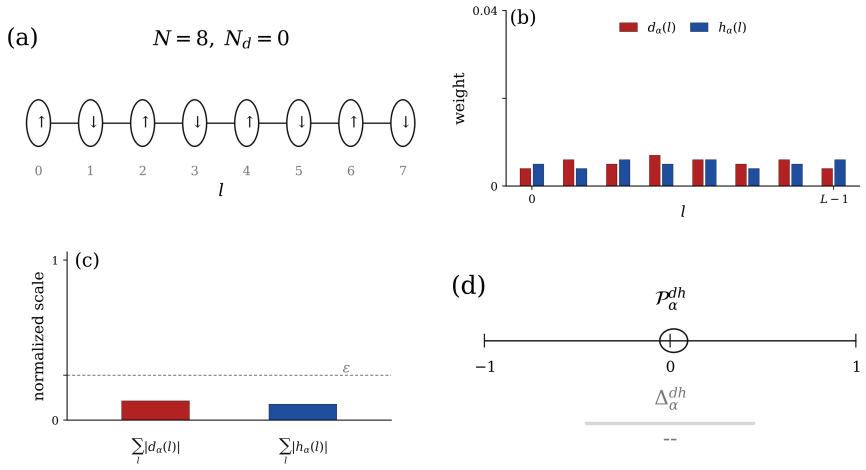

Figure 3. Lack of defect polarization in the half-filled no-pair sector. Low doublon and holon weights, balanced particle distribution along the chain, and negligible connected covariance suggest a charge-inert Mott-like sector rather than a hidden boundary-localized excitation.

It is crucial to note that absence of density imbalance is meaningful only after analysis of the defect-resolved properties. Right-eigenvector analysis may imply weak boundary amplification, but biorthogonality shows that there is no stable defect excitation to polarize. This establishes the no-pair sector as a reference state to compare against.

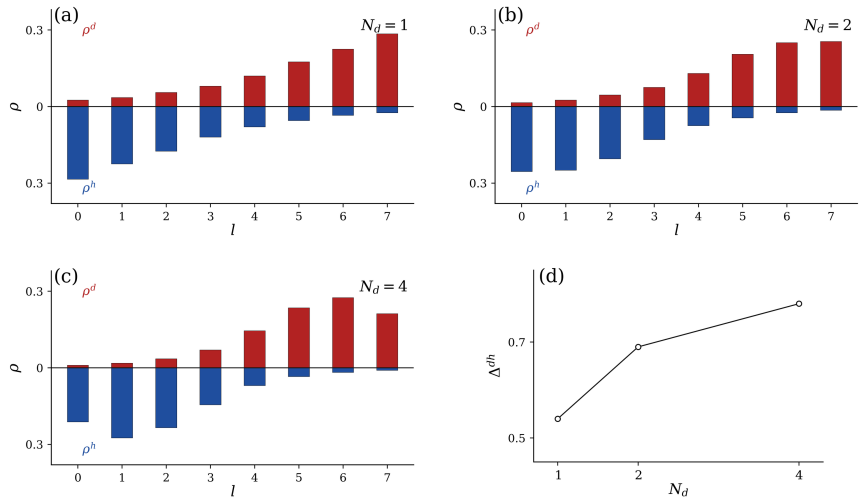

Figure 4. Emergence of boundary-stretched doublon–holon dipoles in sectors carrying defects. Normalized doublon and holon densities become localized around opposite ends of the chain, which demonstrates that the skin signal comes from internal dipole polarization of defects rather than simply from accumulation of the charge.

5.2 Doublon–holon pair sectors and emergence of stretched boundary dipoles

In contrast, when charge defects appear, the picture dramatically changes. Doublons and holons can hop away from each other while retaining correlation due to the many-body structure. As a consequence, they form a dipole: one defect type becomes concentrated at one end of the chain and another defect at the other end. The key is that this polarization and separation are local manifestations of collective skin response.

Figure 4 compares representative one-pair, two-pair, and multiple-pair sectors. Doublon and holon densities become more and more localized near the chain boundaries with increasing pair content. Both the separation and dipole measures confirm that there is stretching of the pair with the increase of its weight. Since the figures are normalized, the emphasis is on spatial separation rather than absolute defect weight.

Figure 4 explains why simple accumulation of total charge can mislead about the skin. Namely, since a doublon and a holon carry opposite deviation from the singly occupied configuration, some of them will partially cancel each other and weaken the imbalance. The defect profiles clearly indicate the dipole polarization.

The third diagnostic tool — the connected covariance — confirms the picture in Figure 4. To be sure about existence of the excitation, the off-diagonal contributions in the covariance need to become significant, indicating that two defects are correlated. This is not possible for independently occurring doublons and holons; only an extended pair excitation can produce it.

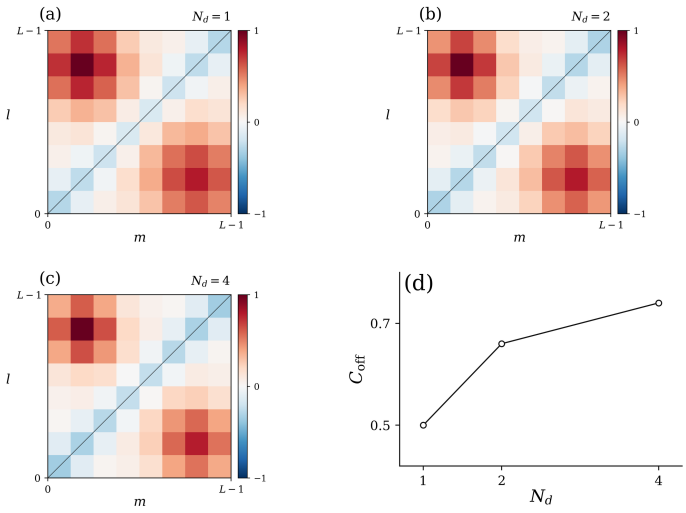

Figure 5. Comparison of connected doublon–holon covariance maps in representative charge sectors. Non-trivial covariance off the diagonal $l = m$ indicates correlation between doublon and holon positions and thus implies collective skin response.

The covariance analysis in Figure 5 corroborates the results in Figure 4. Even in case of clear separation, it was impossible to say whether it was caused by correlation or independent preference. Only connected covariance makes sure that there is correlation between defects; namely, the chain hosts a composite skin localized excitation.

5.3 Switching of the transition from smooth imbalance to staircase sectors with growing interaction

Whether the doublon–holon content defines a clearly visible sector depends on the interaction strength. When $U/t = 0$, there is no cost for switching the local double occupancy. Thus, the eigenstate spectrum includes a superposition of all charge configurations, and the imbalance distribution appears smooth since individual states can continuously adjust their boundary responses without developing steps. For large enough on-site Coulomb energy, such as at $U/t = 10$, the state spectrum becomes sorted according to the doublon number, and the imbalance shows up as a staircase structure.

Figure 6 demonstrates this transition effect. The weak-coupling curve has to be interpreted as a response involving multiple charge-defect sectors mixed together. In turn, the interaction-strengthened pattern must be understood in terms of successive charge-defect sectors determined by increasing numbers of doublons and holons. The stair-like structure of the pattern is entirely due to the presence of each doublon–holon pair contributing another boundary-active internal degree of freedom.

In other words, while the increase in correlation reduces charge mobility in the bulk, it first eliminates incoherent mixing and subsequently makes the remaining charge-defect states more distinct. As a result, the same repulsive interaction that suppresses transport processes at the Fermi energy also sharpens the skin response of the charge excitations. This double

effect explains why the no-pair sector produces a relatively weak polarizing skin signal while finite-pair sectors show distinct steps.

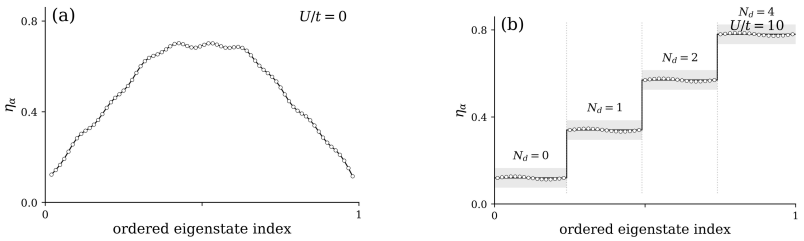

Figure 6. Organization of the boundary imbalance driven by interaction. In the weak-coupling regime, the response remains smooth as a result of high mixing among charge-defect sectors. At $U/t = 10$, the boundary imbalance becomes resolved as steps associated with the corresponding numbers of doublon–holons.

Table 2. Explanation of the principal observables utilized in the skin response analysis. The table serves as a guide for reading Figs. 3–9.

Observable	Large or structured value suggests	Interpretation of this observable in this work
$\rho^{d}_{\alpha}(l)$ and $\rho^{h}_{\alpha}(l)$	Localized charge densities of doublon and holon states in distinct chain halves	The skin response is formed by localized charge defects.
$\mathcal{P}^{dh}_{\alpha}$	Asymmetry of the distributions of doublon and holon states	The charge-excited state possesses a dipolar skin configuration.
Δ^{dh}_{α}	Large distance between doublon and holon distributions	Internal coordinate of the excitation is stretched across the chain ends.
$\mathcal{C}^{dh}_{\alpha}(l, m)$	Off-diagonal charge correlation function of doublon and holon distributions	Two separated states belong to a correlated charge defect excitation.
η_{α}	Density asymmetry between the two ends of the chain	Conventionally defined skin signal. To be considered after defect decomposition.
$\Theta_{\alpha}(E_p)$	Winding about a point gap under branch insertion of flux quantum	The skin defect exhibits complex flux-induced spectral torsion.

Table 2 helps interpret the results reported in the Results Section. No single observable is sufficient by itself. The strongest evidence of collective skin localization occurs when the defect asymmetry, covariance, imbalance, and flux torsion agree in a single charge-defect sector. Such a condition becomes particularly important for finite system studies, where a single observable may be affected by normalization or sector hybridization.

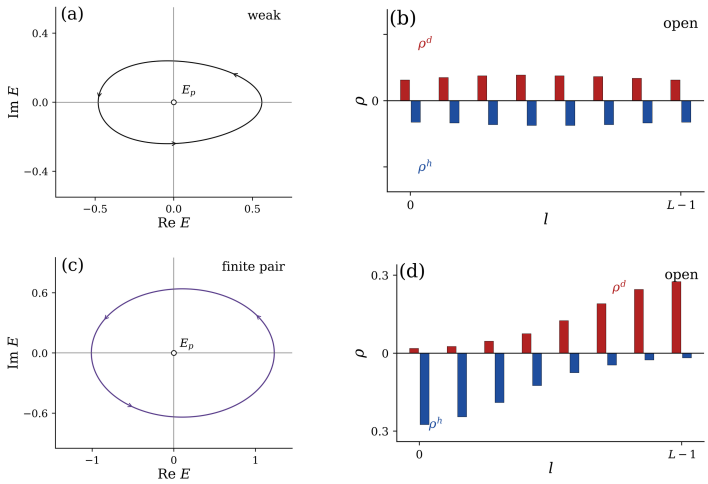

Figure 7. Comparison between flux-induced complex torsion and open-boundary dipole texture. Complex eigenvalues under twisted boundaries are compared with their boundary-active doublon–holon profiles and covariance matrices at the representative value of interaction.

5.4 Torsion through flux and mapping between spectral complex motions and open-boundary textures

The open-boundary technique produces a picture of spatial textures, while the skin effect is also inherently spectral. To link this perspective, some representative eigenvalue branches are tracked by twisting the boundary flux ϕ from zero to 2π. A branch wrapping around the point gap serves as an example of complex torsion. However, if the same branch also features a stretched doublon–holon texture in the open-boundary geometry, there is agreement between spatial and spectral descriptions.

Figure 7 provides the evidence of a direct mapping between complex motions under flux insertion and boundary defects textures under open boundaries. The key insight is not only that complex loops are indeed present in the spectral space but that each loop corresponds to a specific excitation sector in terms of local excitations.

Figure 7 shows how the paper makes use of branch-resolved information rather than a global spectral winding of the determinants over the entire many-body spectrum. Otherwise, an investigator cannot determine which defect texture is responsible for complex torsion.

5.5 Interaction-induced reorganization of exceptional states

An increase in the ratio of U/t can make complex conjugate branches converge, collapse into exceptional states, and split into real branches again. Such a reorganization occurs when the eigenvectors become highly dependent. It becomes difficult to track branch identity smoothly through an exceptional point, hence the necessity to consider both spectral information and covariance textures at the same time.

Figure 8 collects three signs of such a reorganization of eigenstates. Namely, a proximity to a convergent point of two complex conjugate branches, a rise in the conditioning index, and a change in covariance texture provide strong evidence of a reorganization.

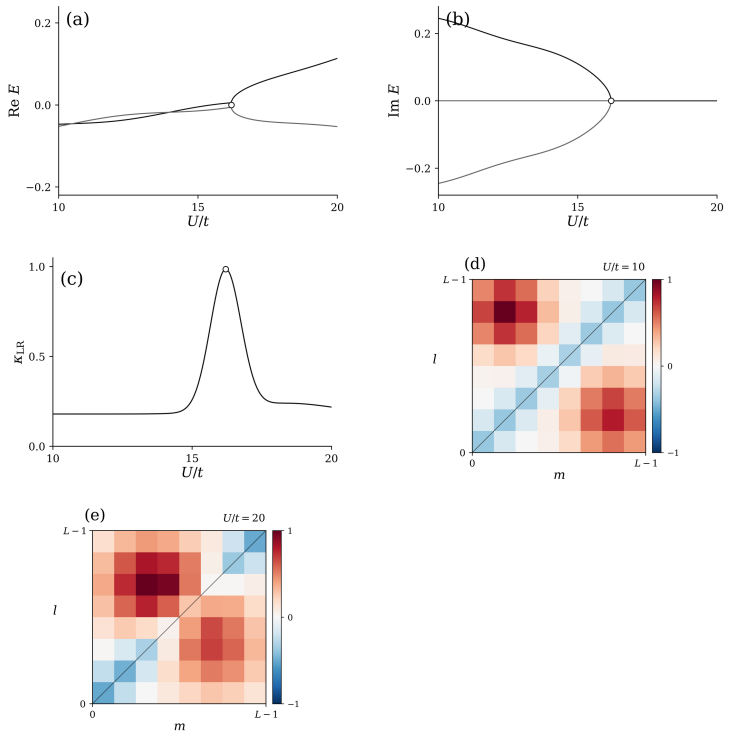

Figure 8. Signatures of interaction-induced exceptional reorganization of branches and their covariance matrices. Two complex conjugate branches move closer to converging into one another, conditioning index increases and, at the same time, the covariance structure changes.

Figure 8 demonstrates that a strong enough interaction tunes the correlated non-Hermitian chain to the edge of exceptional regions. In particular, an eigenstate before the exceptional region has the property of carrying both complex motion under twisted boundaries and boundary-stretched covariance matrix. However, in the vicinity of the exception or right after it, the same state loses the former or gains the latter property. Strong interaction thus restructures the entire basis of eigenstates.

5.6 A doped chain and odd imbalance series

A $N = 7$, $L = 8$ chain with no additional doublon–holon pairs contains an unpaired holon. Since there is no vacancy or overfilling of any site at half filling, the ground state at such parameters was charge-inert. With the chain doped with a holon, the unpaired particle is already a charge defect. Nonreciprocity can act on it without having to form a neutral pair.

Figure 9 shows how this situation leads to the emergence of a new first term of the sequence. Without the additional pairs, only the unpaired defect contributes to the total number of boundary-active dipoles. With one doublon–holon pair introduced into the system, two extra dipole components arise and further pairs add to this composite structure.

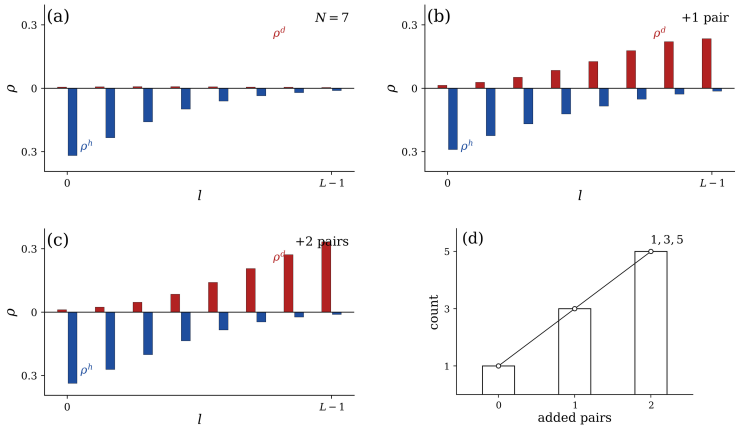

Figure 9. Doping shifts the first term of the boundary-active defect sequence. There is a doped holon contributing to the sequence before the appearance of any pairs, hence the odd first term.

Figure 9 clears up a potential ambiguity that could have occurred in the previous discussion of boundary responses in a half-filled chain. Namely, a mere scaling of density imbalance would occur if the boundary response depended solely on the number of electrons. Instead, the doublon–holon decomposition demonstrates that there is an additional mechanism, the doped defect channel.

5.7 Implications for new technology and materials

The results are relevant to new technology and materials, as they highlight how one can engineer boundary localization via combined control over non-reciprocal transport, interaction strength, and filling. Cold atoms in optical lattices have already been shown to realize Hubbard physics while being capable of providing site-resolved data on empty, singly occupied, and doubly occupied states [20–22]. Photonic, electrical, acoustic, and mechanical systems can generate non-reciprocal couplings and modes that accumulate near boundaries in response to boundary texture, despite replacing doublons and holons with their platform-specific counterparts [5, 6, 23].

The central conclusion concerning material design is that correlations provide additional degrees of freedom in designing a non-Hermitian system, rather than simply complicating the picture. An increased value of U/t reduces low-energy charge excitations but enhances separation between different charge defect sectors. Doping adds the single-defect channel, which can exist alongside a pair-induced dipole channel. Finally, flux control offers a way to detect which of the sectors and defects is involved in spectral complexity. A realistic device or simulator built along the outlined principles would thus not focus on maximization of the global boundary accumulation, but would rather pick up the specific excitation whose defect profile, covariance, and branch structure correspond to the desired response.

6 Conclusions

In this work, we have posed the question whether non-reciprocal collective skin localization in an interacting system can be identified based on state-resolved biorthogonal dipole response, rather than relying exclusively on a global spectral feature. Our results indicate that this is indeed possible. Although the presence of a gap or a branch-winding flux in a many-body spectrum is a required condition of non-Hermitian topology identification, the state-specific excitation response is needed to reveal which actual physical excitation carries the open-boundary response. Biorthogonal tomography for the doublon and holon defect channels presented in this study provides that missing piece of information.

Our analysis has shown that the half-filled no-pair sector remains weakly polarized, as it involves no robust real

charge defect. On the contrary, non-trivial doublon-holon sectors give rise to stretched boundary dipole responses whose local defect profile, separation index, and covariance map characterize the associated composite skin-carrying excitation. Weak interaction causes the imbalance to change smoothly, since there is a strong mixing of charge defect sectors. For stronger interaction ($U/t = 10$), the imbalance staircase is determined by separation between sectors and conversion of charge defects into a pair-driven response. Twisted boundary conditions also lead the same sectors and defects to exhibit complicated branch structure. The interplay of interactions and exceptional state reorganization has caused changes in both branches and local covariance, indicating that even the full set of eigenstates can be reconstructed via correlation properties. Doped $N = 7$ spinless chain has been found to involve an unpaired holon which contributes a single-defect skin channel before introducing further pairs, thus explaining the unique pattern of skin defects.

To summarize, we have provided a definitive answer to the posed research question: in the non-reciprocal Hubbard chain, the excitation carrying the skin effect is characterized by four criteria - separated doublon-holon defect profiles, finite dipole/separation response, off-diagonal connected covariance, and branch-resolved flux torsion.

As for the methodology, we have proposed a diagnostic protocol for detecting skin localization in an interacting non-Hermitian many-body system: choose an excitation sector, determine the biorthogonal defect observables, check their off-diagonal covariance, and verify that the chosen branch undergoes winding under flux insertion. The protocol can be applied to larger chain sizes, finite temperature ensembles, tensor network calculations, and dissipative Liouvillean models, as well as to other materials and synthetic systems in which the relevant skin channel is associated with composite defects or correlated modes rather than bare particles. Thus, our conclusions suggest that future non-reciprocal quantum materials and simulator design should consider not only the spectral topology, but also the excitation regime at hand.

Data availability

All of the presented data are produced as a result of the finite-size calculations for non-reciprocal Hubbard chains. All observables were calculated according to the formulae in Section 4. Each panel represents a state-resolved defect profile, covariance map, imbalance dependence, or flux evolution of either one of the branches of the many-body spectrum.

Conflict of interest

Author has declared no conflict of interest.

References

[1] C. M. Bender, Making sense of non-Hermitian Hamiltonians, *Reports on Progress in Physics* 70 (2007) 947–1018.

[2] A. Mostafazadeh, Pseudo-Hermiticity versus PT symmetry: The necessary condition for the reality of the spectrum of a non-Hermitian Hamiltonian, *Journal of Mathematical Physics* 43 (2002) 205–214.

[3] R. El-Ganainy, K. G. Makris, M. Khajavikhan, Z. H. Musslimani, S. Rotter, and D. N. Christodoulides, Non-Hermitian physics and PT symmetry, *Nature Physics* 14 (2018) 11–19.

[4] Y. Ashida, Z. Gong, and M. Ueda, Non-Hermitian physics, *Advances in Physics* 69 (2020) 249–435.

[5] E. J. Bergholtz, J. C. Budich, and F. K. Kunst, Exceptional topology of non-Hermitian systems, *Reviews of Modern Physics* 93 (2021) 015005.

[6] R. Lin, T. Tai, L. Li, and C. H. Lee, Topological non-Hermitian skin effect, *Frontiers of Physics* 18 (2023) 53605.

[7] N. Hatano and D. R. Nelson, Localization transitions in non-Hermitian quantum mechanics, *Physical Review Letters* 77 (1996) 570–573.

[8] N. Hatano and D. R. Nelson, Non-Hermitian delocalization and eigenfunctions, *Physical Review B* 58 (1998) 8384–8390.

[9] S. Yao and Z. Wang, Edge states and topological invariants of non-Hermitian systems, *Physical Review Letters* 121 (2018) 086803.

[10] K. Yokomizo and S. Murakami, Non-Bloch band theory of non-Hermitian systems, *Physical Review Letters* 123 (2019) 066404.

[11] N. Okuma, K. Kawabata, K. Shiozaki, and M. Sato, Topological origin of non-Hermitian skin effects, *Physical Review Letters* 124 (2020) 086801.

[12] K. Kawabata, K. Shiozaki, and S. Ryu, Many-body topology of non-Hermitian systems, *Physical Review B* 105 (2022) 165137.

[13] S.-B. Zhang, M. M. Denner, T. Bzdusek, M. A. Sentef, and T. Neupert, Symmetry breaking and spectral structure of the interacting Hatano–Nelson model, *Physical Review B* 106 (2022) L121102.

[14] F. Alsallom, L. Herviou, O. V. Yazyev, and M. Brzezinska, Fate of the non-Hermitian skin effect in many-body fermionic systems, *Physical Review Research* 4 (2022) 033122.

[15] B. H. Kim, J.-H. Han, and M. J. Park, Collective non-Hermitian skin effect: Point-gap topology and the doublon–holon excitations in non-reciprocal many-body systems, *Communications Physics* 7 (2024) 73.

[16] S. Longhi, Spectral structure and doublon dissociation in the two-particle non-Hermitian Hubbard model, *Annalen der Physik* 535 (2023) 2300291.

[17] P. Brighi and A. Nunnenkamp, Nonreciprocal dynamics and the non-Hermitian skin effect of repulsively bound pairs, *Physical Review A* 110 (2024) L020201.

[18] C. Rangi, J. Moreno, and K.-M. Tam, Interplay of non-Hermitian skin effect and electronic correlations in the non-Hermitian Hubbard model via real-space dynamical mean-field theory, *arXiv:2507.19471* (2025).

[19] D. C. Brody, Biorthogonal quantum mechanics, *Journal of Physics A: Mathematical and Theoretical* 47 (2014) 035305.

[20] W. S. Bakr, J. I. Gillen, A. Peng, S. Foelling, and M. Greiner, A quantum gas microscope for detecting single atoms in a Hubbard-regime optical lattice, *Nature* 462 (2009) 74–77.

[21] J. F. Sherson, C. Weitenberg, M. Endres, M. Cheneau, I. Bloch, and S. Kuhr, Single-atom-resolved fluorescence imaging of an atomic Mott insulator, *Nature* 467 (2010) 68–72.

[22] P. M. Preiss, R. Ma, M. E. Tai, A. Lukin, M. Rispoli, P. Zupancic, Y. Lahini, R. Islam, and M. Greiner, Strongly correlated quantum walks in optical lattices, *Science* 347 (2015) 1229–1233.

[23] T. E. Lee, Anomalous edge state in a non-Hermitian lattice, *Physical Review Letters* 116 (2016) 133903.